

Passive freeze-out of the Richtmyer-Meshkov instability

J. Strucka,^{1,*} D. M. Sterbentz,² B. Lukic,³ K. Mughal,¹ Y. Yao,¹ K. Marrow,¹ W. J. Schill,² C. F. Jekel,² D. A. White,² N. Asmedyanov,⁴ R. Grikshtas,⁴ O. Belozerov,⁴ S. Efimov,⁴ J. Skidmore,⁵ A. Rack,³ Ya. E. Krasik,⁴ J. L. Belof,² J. P. Chittenden,¹ and S. N. Bland¹

¹*Plasma Physics Group, Imperial College London, London SW7 2BW, United Kingdom*

²*Lawrence Livermore National Laboratory, Livermore, California 94550, USA*

³*ESRF - The European Synchrotron, CS 40220, 38043 Grenoble Cedex 9, France*

⁴*Physics Department, Technion-Israel Institute of Technology, Haifa 32000, Israel*

⁵*First Light Fusion Ltd., Oxford Industrial Park, Yarnton OX5 1QU, United Kingdom*

(Dated: February 26, 2026)

The Richtmyer-Meshkov instability (RMI) poses a major challenge in inertial confinement fusion (ICF) due to its role in mixing and performance degradation. We report the first experimental observation of passive freeze-out of RMI in a low-pressure surrogate regime; an instability stagnation effect induced without modifying the driving pressure pulse or the target surface geometry. Using additively manufactured sub-surface voids in a sinusoidal target, we convert a single shock into a sequence of weaker shocks that suppress instability growth upstream of the surface by over 70%. High-speed X-ray imaging and hydrodynamic simulations suggest that this suppression arises primarily from temporal shaping, with lesser contributions from spatial curvature and shock weakening. Our results demonstrate a driver-independent pathway for controlling shock-driven hydrodynamic instabilities relevant to ICF and other high energy density systems.

The Richtmyer-Meshkov instability (RMI) arises when an interface between fluids of differing densities undergoes impulsive acceleration, typically from shock waves [1, 2]. This triggers dynamics such as interface distortion, jetting, and uncontrollable fluid mixing regardless of the initial density configuration. Controlling RMI is essential for uniformity in compression experiments and inertial confinement fusion (ICF), as recently demonstrated by the success at the National Ignition Facility [3]. In ICF, the instability drives mixing of high- Z materials from outer layer of the fuel capsule into the fusion fuel. Such impurities radiate energy efficiently, lowering the core fuel temperature and ultimately halting the thermonuclear reaction [4, 5]. This letter reports experimental observation of passive freeze-out, a phenomenon based on a prediction first made by Mikhaelian 40 years ago [6]. Namely, we show that the temporal structure of a pressure pulse generated by the shock-sample interaction can self-suppress RMI. This effect opens a new class of alternative strategies aimed at mitigating instabilities, alongside graded density transitions [7], reverberation waves across multiple interfaces [8], tailored shock wave pairs [9], magnetic stabilization in plasmas [10, 11], and radiative stabilization [12].

While nearly ideal initial conditions would also prevent instability growth, achieving such symmetry is impractical in most scenarios [13]. For instance, in multi-shell direct-drive ICF, maintaining near-spherical capsule symmetry requires adhesive-filled joints [14–16]. In indirect-drive ICF, fill-tubes and foam structures are used to inject and soak deuterium-tritium fuel into the capsule. These necessary features act as hydrodynamic

defects which seed instabilities and demand advanced mitigation strategies to limit mixing. Reflecting this ongoing challenge, recent studies have closely examined various aspects of fill-tube dynamics [17–20] and isolated defects [21, 22]. In a surrogate, low-pressure regime, we demonstrate passive stabilization of a shock-compressed sinusoidal interface through introduction of numerically optimized voids. These structures shape the shockwave without placing constraints on the driving technology, suggesting a route toward mitigating instabilities seeded by fill tubes, joints, and other unavoidable perturbations.

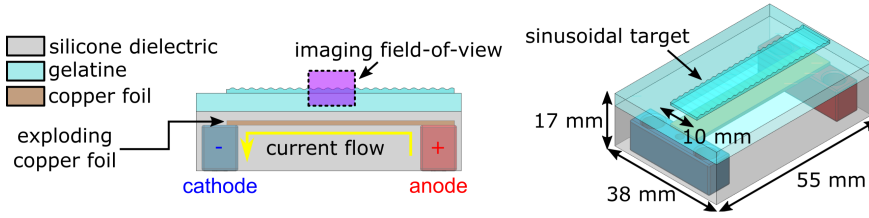
The experiment is illustrated in Fig. 1(a). Two sample geometries were compressed by a shock wave ($P_{\max} \approx 500$ MPa) generated by the electrical explosion of a copper foil: a sinusoidal interface (wavelength $\lambda = 0.95$ mm, amplitude $a_0 = 0.1$ mm), and a sinusoidal interface with void structures located under the surface for instability suppression. The experiments were performed in air with a density contrast at the perturbed interface given by the Atwood number $A = (\rho_{\text{air}} - \rho_{\text{g}})/(\rho_{\text{air}} + \rho_{\text{g}}) \approx -1$, where ρ_{air} and ρ_{g} represent the densities of air and gelatine, respectively. Two-dimensional hydrodynamic simulations informed the suppression void design using the trust region Bayesian optimization method [23]. The voids were parameterized by four piecewise cubic Hermite polynomials constrained to be within a range of [0.06, 0.134] cm from the interface [24]. The optimization varied these polynomials to minimize the objective function:

$$\phi = \text{Max} \left(\frac{1}{N_r} \sum_{i=1}^{N_r} |h_{\text{p},i} - h_{\text{b},i}| \right). \quad (1)$$

Here, $h_{\text{p},i}$ denotes the instability amplitude (“jets”), $h_{\text{b},i}$ the trough amplitude (“bubbles”), and N_r the number of perturbation periods. Eq. 1 represents the maximum mixing zone width obtained within the simulation for

* jergus.strucka15@imperial.ac.uk

(a) side-on and 3D view of the sample



(b) sample geometry

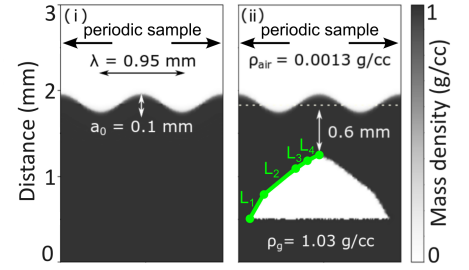


FIG. 1. (a) Side-on and isometric view of the experimental setup showing the exploding copper foil, direction of the current flow, and sample geometry. (b) Initial conditions of the baseline (i) and instability mitigation (ii) sample geometry. Functions L_i correspond to linear functions that approximate the optimal void geometry that is detailed in the Methods section.

a specific geometry. To simplify fabrication, the optimal geometry was approximated using four linear segments (L_1 , L_2 , L_3 , and L_4). Additional simulations confirmed that this approximation preserved the suppression dynamics. The approximated geometry is shown in Fig. 1(b, ii). Fig. 2 shows the compression and instability dynamics observed using a sequence of time-resolved X-ray radiographs ($\bar{E} = 30$ keV, pulse length ~ 60 ps) at the European Synchrotron. More details about the setup and simulations are provided in the appendices.

Fig. 2(a) shows the baseline RMI. The driving shock-wave propagated through the gelatine sample at $v_{\text{shock}} = 2.2 \pm 0.2$ km s $^{-1}$ (Mach 1.5). By $t = 2.6$ μ s, the sinusoidal interface was compressed, inverted, and generated strong jetting, consistent with dynamics expected at highly negative Atwood numbers and previously observed in laser experiments [25]. Between 0.5 and 5 μ s, the interface of the baseline experiment advanced at $v_{\text{base}}^{\text{mean}} = 316 \pm 10$ m s $^{-1}$, while the jet tip propagated at $v_{\text{base}}^{\text{jet}} = 651 \pm 25$ m s $^{-1}$. In comparison, the suppression geometry in Fig. 2(b) exhibits significantly reduced instability and jetting. Three intensity regions are observed: the thick gelatine substrate required for fabrication of the suppression sample (~ 50 mm into the page, dark, not present in baseline), the suppression sample (~ 10 mm, gray), and the overlying air (bright). Between $t = 0.3$ μ s and 1.3 μ s, increased attenuation within the engineered void indicates its crushing, followed by the emergence of an upward-propagating, two-lobed bubble structure that dominates the dynamics for $t > 2$ μ s. High-resolution radiographs and simulations show that this structure originates from jetting at the void corners. After inversion, upward-directed jets form from the initial troughs of the sinusoidal surface. The interface, defined by X-ray transmission $T < 0.95$, advances at $v_{\text{supp}}^{\text{mean}} = 320 \pm 13$ m s $^{-1}$, with jet tips propagating at a much reduced speed $v_{\text{supp}}^{\text{jet}} = 407 \pm 19$ m s $^{-1}$.

An imprint of the initial void appears in all radiographs of the suppression dynamics. This originates from ~ 100 μ s X-ray pre-illumination of the LYSO:Ce scintillator, which induces a slowly decaying, spatially non-uniform increased conversion efficiency reflecting the ini-

tial transmission rather than a true double exposure. For $t = 2.7$ μ s and 5 μ s, true features are highlighted with green dashed lines to distinguish them from the gradually fading imprint.

There are three mechanisms that can contribute to the observed instability suppression: (1) attenuation of the driving shock wave by the void, (2) temporal shaping of the pressure pulse via conversion of a single strong shock into multiple weaker shocks, and (3) spatial shaping of the shock front, which modifies baroclinic vorticity deposition at the interface through $\nabla\rho \times \nabla p$. Fig. 3 presents numerical simulations that reproduce the overall dynamics observed in the X-ray radiographs, including void collapse and mixing-zone evolution. Residual differences, such as the apparent jet thickness, are conjectured to arise primarily from line-of-sight integration through the finite sample thickness, alignment, and imperfect surface finish. In the following, we assess the relative contributions of each mechanism using numerical simulations and growth-rate measurements from X-ray imaging (Fig. 4).

Attenuation: For sufficiently small perturbation amplitudes ($a(t_0)/\lambda \ll 1$), the contribution of shock attenuation to the RMI suppression can be estimated using the linear growth rate [1]:

$$\frac{da(t)}{dt} = \frac{2\pi}{\lambda} a(t_0) A \Delta u, \quad (2)$$

where $a(t)$ and λ are the perturbation amplitude and wavelength, A is the Atwood number, and Δu is the free surface velocity after shock compression. From Fig. 2, we measure mean position of the interface and its velocity v_i^{mean} which corresponds to Δu in Eq. 2. The perturbation growth $da(t)/dt$ corresponds to the jetting speed in the free surface frame given by $v_i^{\text{jet}} - v_i^{\text{mean}}$. In linear regime, dividing Eq. 2 by Δu yields the ratio $\beta_i = (v_i^{\text{jet}} - v_i^{\text{mean}})/v_i^{\text{mean}} = 2\pi a(t_0) A/\lambda$ which depends only on the initial geometry. Thus, any reduction in jetting (lower $v_i^{\text{jet}} - v_i^{\text{mean}}$) due to shock attenuation (lower v_i^{mean}) should yield the same β parameter. Measurements in Fig. 4 indicate that $\beta_{\text{base}} = -1.06 \pm 0.1$ for the baseline geometry and $\beta_{\text{supp}} = -0.27 \pm 0.08$ for

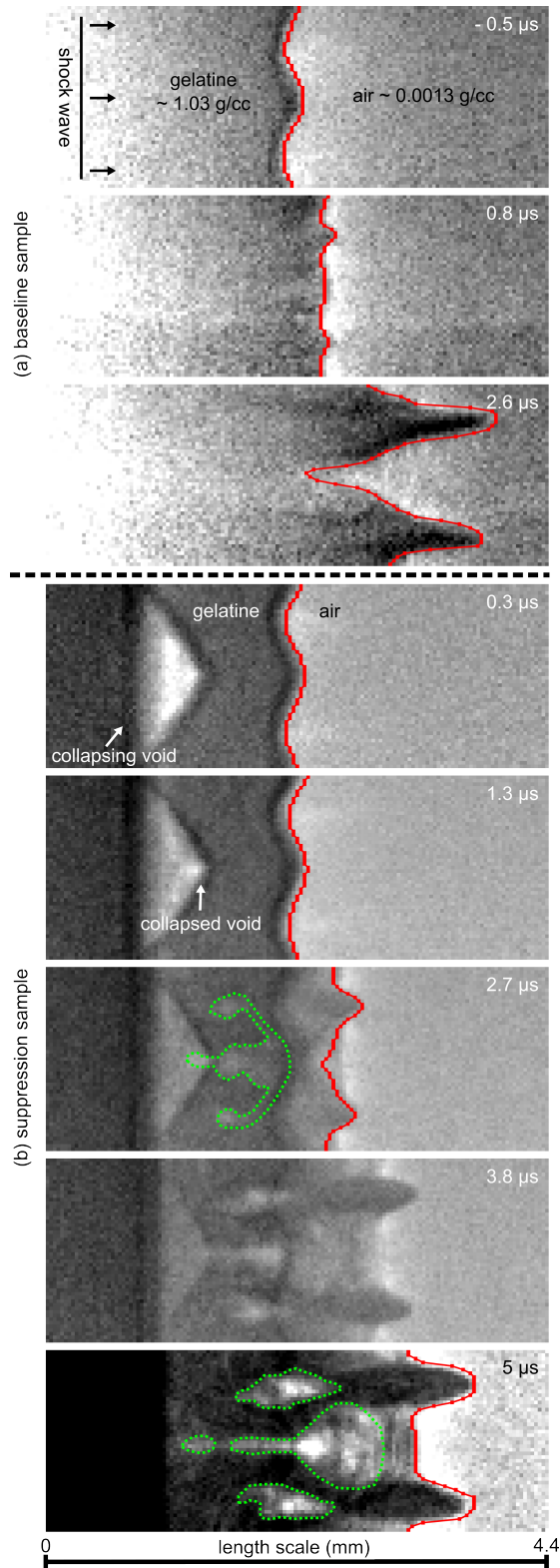


FIG. 2. (a) X-ray radiographs of our baseline experiment showing shock compression of a sinusoidal surface. (b) Sequence of radiographs showing compression of the instability suppression sample. Green dashed lines highlight void structures while red lines show tracked interfaces.

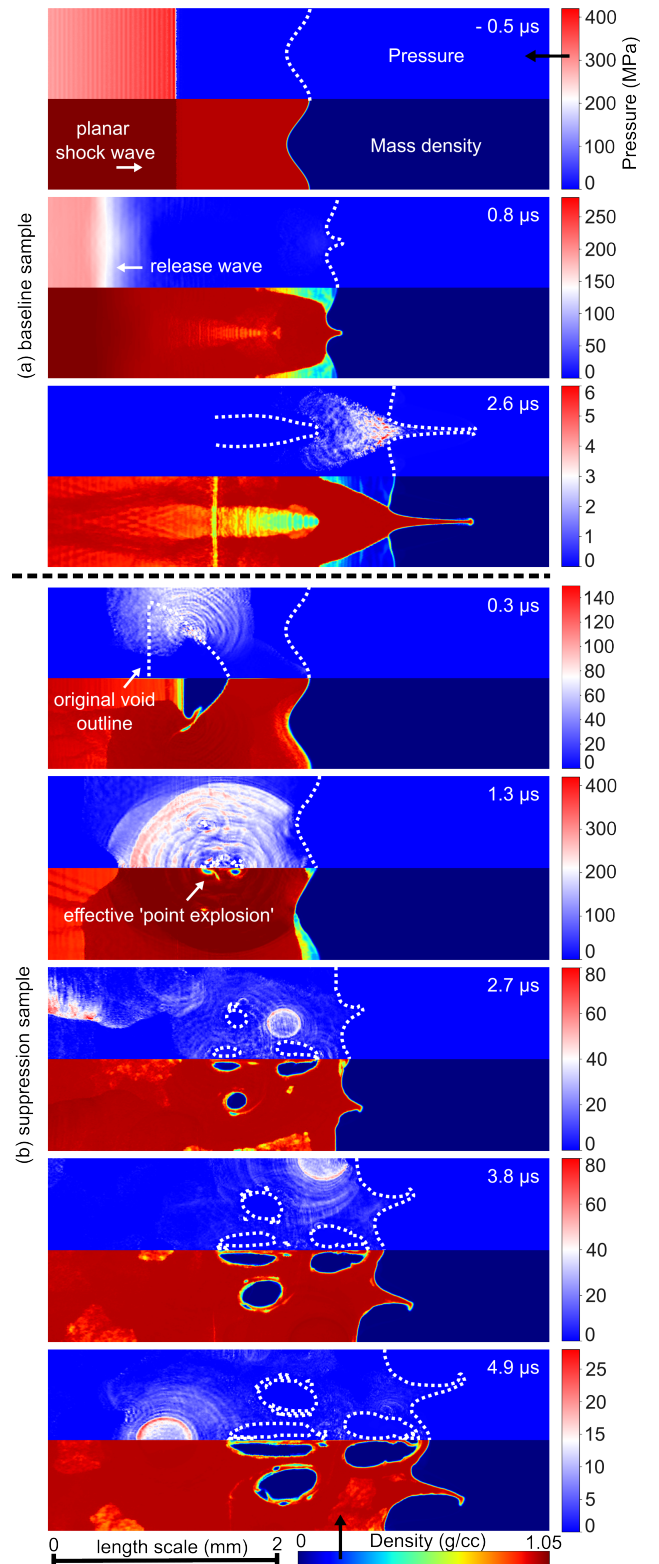


FIG. 3. (a) Simulated pressure and density fields for the baseline scenario. (b) Corresponding fields from the instability suppression case, highlighting key dynamics. In each plot, the top half shows pressure, and the bottom half shows density. Pressure plots include white dashed contours indicating material interfaces or strong density gradients. Note: To highlight features, the pressure color bars vary between plots.

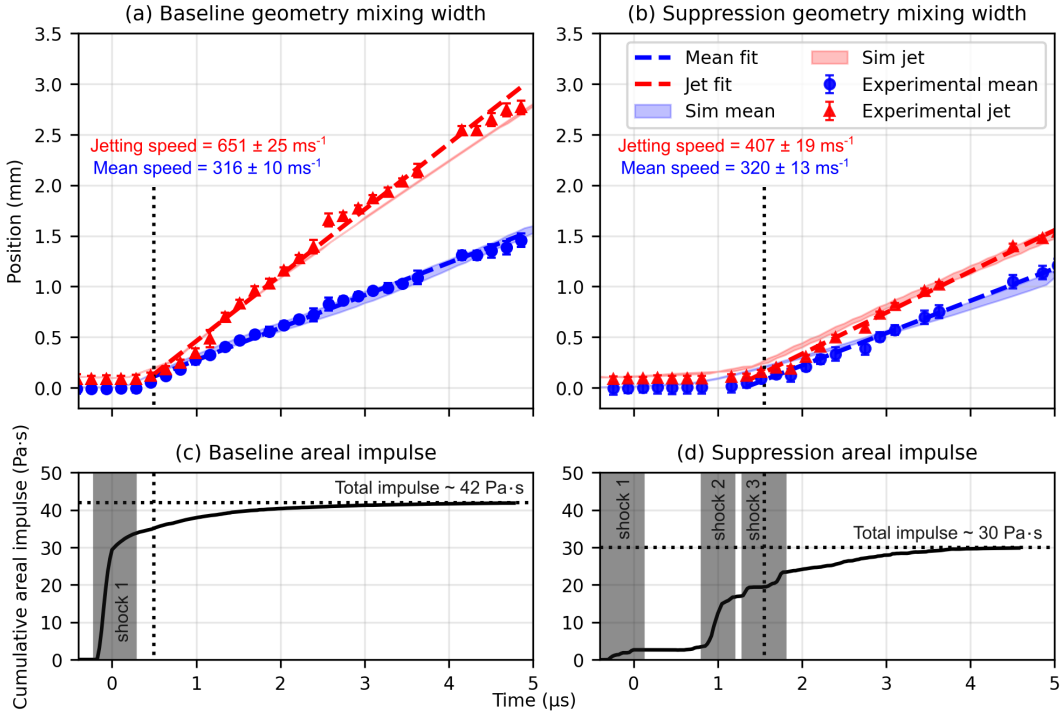


FIG. 4. (a) Jet tip position (red) and mean interface position (blue) vs. time for the baseline geometry. (b) Same as (a), for the suppression geometry (c) Integrated areal impulse delivered to the gelatine–air interface in the baseline case. (d) Same as (c), for the suppression case. The dashed vertical line indicates the time of interface inversion in all subplots.

the suppression geometry. While the initial conditions are weakly nonlinear, the large difference in β parameters suggests that pure shock attenuation cannot explain the observed reduction in jetting. Nonetheless, numerical simulations show that the areal impulse imparted to the interface decreases from $42 \text{ Pa}\cdot\text{s}$ to $30 \text{ Pa}\cdot\text{s}$ when moving from the baseline to the suppression geometry. This indicates that some, but not all, reduction is due to partial decoupling of the shock from the interface due to the void structure.

Temporal shaping: Over 40 years ago, Mikhaelian suggested that shaping the pressure pulse in time, for example by delivering two equally strong planar shocks at two distinct times when the interface amplitude is $a(t_1) = a_0$ and $a(t_2) = -a_0$, can fully suppress linear RMI in negative Atwood number configurations [6].

Fig. 3 shows the simulated pressure and density distribution in the baseline and suppression geometries at four key times, while Figs. 4(c,d) show the cumulative impulse history experienced by the gelatine–air interface extracted from these simulations. In the suppression case in Fig. 3, we observe that crushing of the void structure converts the initial pressure profile from a single shock into a sequence of weaker shocks arriving at the interface at various stages of RMI. Simulations show three dominant shocks impacting the interface, the first at $t_1 \approx 0.25 \mu\text{s}$ with $a(t = t_1) = 100 \mu\text{m}$, $P_1 \approx 35 \text{ MPa}$,

and impulse $I_1 = 1.6 \text{ Pa}\cdot\text{s}$. The second follows at $t_2 \approx 1.25 \mu\text{s}$ with $a(t = t_2) = 100 \mu\text{m}$, $P_2 \approx 255 \text{ MPa}$, and $I_2 = 19.4 \text{ Pa}\cdot\text{s}$; the third at $t_3 \approx 1.75 \mu\text{s}$ with $a(t = t_3) = 0$, $P_3 \approx 40 \text{ MPa}$, and $I_3 = 4.88 \text{ Pa}\cdot\text{s}$. Figs. 4(c,d) show the corresponding time-resolved areal impulse distributions. The inversion time of the interface, i.e. $a \approx 0$, is delineated by vertical dotted lines.

The effect of this multiple shock structure on the dynamics can be estimated using linear theory in Eq. 2 by treating the total jetting as a linear sum of individual contributions from the three main shocks:

$$\left. \frac{da(t)}{dt} \right|_{\text{shocks}} = \frac{2\pi}{\lambda} \sum_n a(t_n) A \Delta u_n, \quad (3)$$

where $a(t_n)$ is the perturbation amplitude at the time of arrival of the n -th shock, and $\Delta u_n = (I_n/I_{\text{tot}})\Delta u$ is the velocity imparted by each shock, scaled according to its contribution I_n to the total impulse I_{tot} . Using this model, the jetting speed is predicted to drop from $v_{\text{base}}^{\text{jet}} = 525 \pm 70 \text{ m s}^{-1}$ in the baseline scenario to $v_{\text{supp}}^{\text{jet}} = 465 \pm 50 \text{ m s}^{-1}$ in the suppression case, with error bars calculated by combining errors in initial geometry ($\sigma_a = 32 \mu\text{m}$, $\sigma_\lambda = 64 \mu\text{m}$) and mean interface speed Δu .

Although simplified, this analysis demonstrates that temporal shaping of shocks interacting with the interface plays a significant role in instability suppression. In practice, the ideal freeze-out may be inaccessible here due to

the asymmetric jetting caused by weakly nonlinear initial conditions, and divergent shock waves produced by effective point explosions. As a result, the baroclinic torque and total momentum transfer is unevenly distributed between the ejected jets and the rest of the interface.

Spatial shaping: The development of a non-planar, curved shock front during the shock-sample interaction can influence instability growth by altering the baroclinic vorticity source term, $\nabla\rho \times \nabla p$. This spatial shaping arises from shock propagation around the void, overlapping shock fronts that create doubly shocked regions, and localized void implosions acting as transient point sources of pressure (see Fig. 3b). Disentangling spatial effects from temporal shaping is nontrivial. Nevertheless, the simulations show that the dominant pressure pulse, generated by the void crushing and subsequent point explosion at $t \approx 1.3 \mu\text{s}$, modifies the vorticity deposited across the perturbation. Specifically, it increases baroclinic torque near the simulation boundaries, where the shock impinges at angles nearly perpendicular to the density gradient, and enhances jetting. Conversely, near the center, where the shock curvature aligns with the interface curvature, this shaping leads to weaker vorticity deposition, producing localized stabilization. The net result of these dynamics is curving of the jets away from the central region. Simulations reveal that the vorticity deposition in the central region between the jets in Fig. 3 is similar across both cases, suggesting that the net effect of spatial shaping in this configuration is not significant.

It should be noted that, while our optimization focused on the evolution of the mixing zone width due to its direct observability in our experiments, the mass modulation, $\delta m(y, t)$, defined as the integrated mass density ρ along the axis of compression, will be equally important in more integrated scenarios. In applications such as ICF, the RMI transitions to Rayleigh-Taylor instability (RTI) as the interface decelerates during compression, where the mass modulation plays a critical role in determining the mixing rate and feedthrough [26, 27], and may compete with early-time stabilization. In Figure 5, we evaluate the normalized mass modulation, $\delta m(y, t) / \langle \delta m_0 \rangle$, from the numerical simulations. Here, $\langle \delta m_0 \rangle$ is the mean areal density at the beginning of the simulation. This modulation is initially higher in the suppression geometry; however, after shock compression, the collapsing voids result in the mass modulation becoming more uniform in the suppression geometry and remains approximately comparable at late time, while simultaneously minimizing long-scale jetting and mix.

In summary, these measurements and simulations demonstrate that growth of the RMI from surface perturbations can be substantially reduced using engineered voids without modifying the surface geometry. In our experiments, we observed suppression of growth in the mixing zone width by over 70% that could be largely explained by temporal shaping of the pressure pulse. Mechanistically, the engineered void acts as a transient energy reservoir, converting a single incident

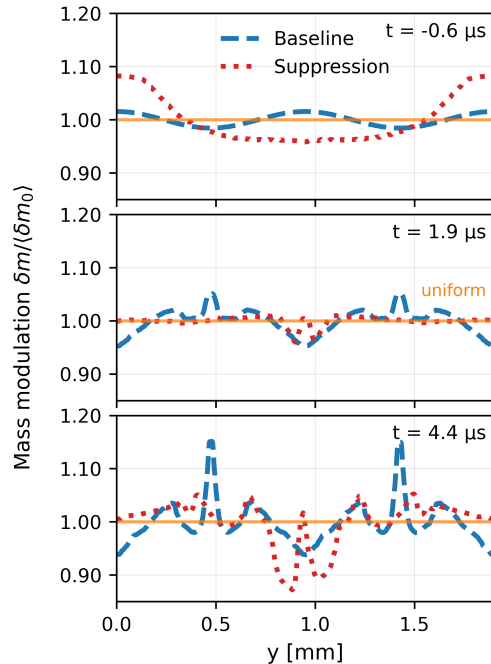


FIG. 5. Mass modulation $\delta m / \langle \delta m_0 \rangle$ at three characteristic times, before shock-compression, shortly after, and at late time. Axis y is perpendicular to direction of compression.

shock into a sequence of pressure pulses—enabling driver-agnostic mitigation of the instability. This approach, alongside novel fabrication methods [28–30], suggests a pathway towards controlling instability growth seeded by hydrodynamic features such as fill tubes or adhesive joints, which are present in inertial confinement fusion and high energy density platforms [13–20]. While the use of shock-cavity interaction to modify pressure distribution appears scalable across multiple pressure regimes [31–33], the void geometry required for each application will vary and require optimization. The dominant role of temporal shaping in suppression observed within our experiments suggests that this method may be only effective for heavy-to-light interface configurations (negative Atwood number), such as internal walls of ICF capsules. Mitigation under light-to-heavy configurations (positive Atwood number) will require further investigation of other strategies such as spatial shock shaping. Finally, more integrated scenarios involving sudden deceleration, such as in ICF, will have to employ a new class of optimization functions suitable for late-time RTI-induced mix, for example, by minimizing mass modulation.

Acknowledgements – This work was supported by EP-SRC and First Light Fusion under the AMPLIFI Prosperity Partnership - EP/X025373/1; the NNSA under DOE DE-NA0004148, Israel Science Foundation Grant No. 418/22, DOE Contract DE-AC52-07NA27344 and the LLNL-LDRD Program Project No. 21-SI-006. The

research was also supported by the ESRF beamtime SC-5443. The Lawrence Livermore National Laboratory journal number is LLNL-JRNL-2010870.

Appendix A: Dynamic compression experiment

The dynamic compression experiment was performed at the European Synchrotron using the ‘‘Grenge’’ pulsed power generator charged to +45 kV [34]. In the experiment, the generator delivered a current pulse of ~ 110 kA in ~ 600 ns into a copper strip encased in dielectric tamp, driving the resistive explosion. The electrical current discharge was measured by a custom-built self-integrating Rogowski coil, and the voltage was measured by a P6015A Tektronix high voltage divider. From the electrical signals, we estimate the total energy deposited into the metallic foil to be ~ 1 kJ in approximately ~ 250 ns as shown in Supplementary Figure A.

The exploding copper strip was 10 mm wide, 40 mm long, and 12.5 μm in thickness. The length and cross-section were chosen by matching the specific current action integral to obtain an almost critically damped discharge [35]. This discharge is characterized by the highest energy coupling efficiency and rate of energy density deposition. At peak current, the copper metal was expected to reach temperatures > 10 kK and consequently thermal pressures in the multi-GPa regime. The high thermal pressure of the exploded foil led to its expansion and a shock wave launch into the dielectric material that was surrounding it. Magnetohydrodynamic simulations of exploding wire arrays performed in the code GORGON estimated peak pressure of the fully formed shock wave at ~ 500 MPa followed by exponential decay to a background of ~ 100 MPa over ~ 5 μs [36]. More details related to this technique and specific driver are given in recent publications [34, 37].

Appendix B: Multi-frame X-ray imaging

The hydrodynamic evolution of the system was measured using ultra-high-speed synchrotron-based X-ray imaging. Approximate layout of the experiment is shown in Supplementary Figure B. The electron bunches stored in the storage ring of the synchrotron passed every 176 ns through two axially aligned long-period undulators ($\lambda_u = 32$ mm). The undulators produced polychromatic X-ray radiation with spectrum spanning 20 – 50 keV (characteristic energy $\bar{E} \approx 30$ keV). The X-rays propagated for 150 m in a vacuum tube before passing through a spectral filter consisting of 1 mm thick Beryllium and ~ 0.8 mm thick Diamond window. The beam then passed through the shock-compressed sample, and another 9 m before impinging on a LYSO:Ce X-ray scintillator (40 ns decay time, Hilger Crystals, UK) that converted the X-ray pulse into visible light. Due to the long propagation distances, the resulting radiographs contained both absorption-based features and edge-enhancement due to propagation-based phase-contrast imaging.

The optical emission from the crystal scintillators was relayed via two pellicle beamsplitters to two Shimadzu HPV-X2 fast-framing cameras operating at 5 MHz. To

capture every X-ray pulse, the cameras operated in parallel with a 100 ns offset. The resulting imaging could obtain up to 256 consecutive radiographs with an effective interframe time of 176 ns (5.68 MHz), exposure time of 100 ns, 8×12.8 mm² field-of-view, and 32 μm resolution.

Throughout the experiments, the X-ray beam was gated by a fast shutter that opened ~ 100 μs prior to the start of measurement. For samples with high absorption contrast, this pre-illumination by multiple synchrotron pulses left a residual, spatially non-uniform conversion-efficiency imprint visible in early frames, as is visible in Fig. 2(b). Additional details regarding the imaging setup can be found in previous publications [37–39].

Appendix C: Sample design and manufacture

All instability samples were manufactured out of gelatine slabs with moulded sinusoidal perturbations (as shown in Figure 1(a) in turquoise color). The mass density of the gelatine was ~ 1.03 g cm⁻³ and yield strength was approximately $Y \sim 10$ kPa [40]. The benefit presented by using gelatine was the simplicity of manufacture of arbitrary shapes using prefabricated metallic / 3D printed plastic moulds, sufficiently high strength to support fixed geometries, but simultaneously sufficiently low strength such that the material behaves hydrodynamically in the experiment.

In all experiments, the sinusoidal interface was manufactured with a wavelength of $\lambda = 0.95 \pm 0.05$ mm and initial amplitude $a_0 = 0.1 \pm 0.02$ mm, setting the dimensionless amplitude to $(2\pi/\lambda)a_0 \approx 0.66$; a regime where the initial dynamics can be weakly nonlinear. Additionally, the Atwood number of the interface between the gelatine ($\rho_0 = \rho_g = 1.03$ g cm⁻³) and the air ($\rho_1 = \rho_{\text{air}} = 0.0013$ g cm⁻³) is $A = -1$, setting the initial conditions in a regime of the parameter space where the resulting dynamics should involve strongly asymmetric peak and trough growth and rapid jetting.

In both the baseline and the suppression geometry, shown in Figure 1(b), the sinusoidal interface was positioned at a distance of ~ 5 mm from the silicone layer and ~ 6 mm from the exploding copper foil.

The only hydrodynamically relevant modification to the suppression geometry consisted of introducing computationally optimized voids behind the interface. The void geometry shown in Figure 1(b)(ii) was used in the experiment. These voids formed a periodic structure repeating every 1.9 mm, with each void described by the following linear functions:

Appendix D: Hydrodynamic simulations

$$I(x) = \begin{cases} 0.5 & \text{for } 0 \leq x < 0.013 \text{ cm} \\ 0.5 + 1.67(x - 0.013) & \text{for } 0.013 \leq x < 0.031 \text{ cm} \\ 0.53 + 0.79(x - 0.031) & \text{for } 0.031 \leq x < 0.073 \text{ cm} \\ 0.56 + 0.63(x - 0.073) & \text{for } 0.073 \leq x < 0.081 \text{ cm} \\ 0.57 + 0.43(x - 0.081) & \text{for } 0.081 \leq x < 0.095 \text{ cm.} \end{cases} \quad (\text{C1})$$

This was an approximation of the optimal design which was prescribed by three piece-wise cubic Hermite interpolating polynomials that are fully defined by the following four points:

$$\begin{aligned} (x_0, y_0) &= (0.0, 0.5) \text{ cm,} \\ (x_1, y_1) &= (0.03167, 0.5014) \text{ cm,} \\ (x_2, y_2) &= (0.06333, 0.5588) \text{ cm,} \\ (x_3, y_3) &= (0.095, 0.5716) \text{ cm.} \end{aligned} \quad (\text{C2})$$

The optimal void geometry was found by using the MARBL hydrodynamics code in combination with trust region Bayesian optimization algorithm. The objective function optimized by the algorithm was the maximum distance between the peaks and the troughs over the entirety of the simulation. This objective function assured that no significant spike growth occurred at any step of the simulation. In total, only 240 runs were required to arrive at the optimal geometry.

All simulated results shown in this publication were obtained by two-dimensional simulations using the MARBL hydrodynamics code; an arbitrary Lagrangian-Eulerian code developed at Lawrence Livermore National Laboratory that uses high-order finite elements to numerically solve conservation equations [41–43]. High-order finite elements are useful for increasing accuracy of the simulations - for instance - by more accurately accounting for deformation at material interfaces. Each of our optimization simulation runs included approximately 16000 elements and was ran for 11 μs , with the final design re-ran at a higher resolution with 60000 elements. A similar simulation method was used in previous work by Sterbentz [24] and compared against the scaling laws developed by Dimonte [44].

We used the Livermore Equation of State (LEOS) library to model the materials in our simulations. As a substitute for gelatine, we used the equation of state of water (dominant component of gelatine, table LEOS 2010). The main discrepancy between these two materials is the slightly higher density of gelatine ($\approx 1.03 \text{ g/cm}^3$). At these low concentrations of gelatine (3%), material strength effects are expected to be minor. Additionally, even if the gelatine is initially solid in the experiment, it is known that at pressures $\gg Y \approx 10 \text{ kPa}$ the gelatine bonds break and the sample liquefies. As such, we typically neglected most strength effects in our simulations with an exception of a simple failure model for the gelatine. This model assumed that failure would occur if compressive stresses were equal to $-(2/3)Y_0$, where we selected $Y_0 = 100 \text{ kPa}$ to match the void structure in the recorded radiographs. Importantly, the jet tip velocity and mean speed in the simulations were largely unaffected by this choice. Material properties of air were modelled using the LEOS 2260 equation of state.

-
- [1] Y. Zhou, Rayleigh–Taylor and Richtmyer–Meshkov instability induced flow, turbulence, and mixing. i, *Physics Reports* **720–722**, 1–136 (2017).
- [2] Y. Zhou, Rayleigh–Taylor and Richtmyer–Meshkov instability induced flow, turbulence, and mixing. ii, *Physics Reports* **723–725**, 1–160 (2017).
- [3] A. B. Zylstra, O. A. Hurricane, D. A. Callahan, A. L. Kritcher, J. E. Ralph, H. F. Robey, J. S. Ross, C. V. Young, K. L. Baker, D. T. Casey, T. Döppner, L. Divil, M. Hohenberger, S. Le Pape, A. Pak, P. K. Patel, R. Tommasini, S. J. Ali, P. A. Amendt, L. J. Atherton, B. Bachmann, D. Bailey, L. R. Benedetti, L. Berzak Hopkins, R. Betti, S. D. Bhandarkar, J. Biener, R. M. Bionta, N. W. Birge, E. J. Bond, D. K. Bradley, T. Braun, T. M. Briggs, M. W. Bruhn, P. M. Celliers, B. Chang, T. Chapman, H. Chen, C. Choate, A. R. Christopherson, D. S. Clark, J. W. Crippen, E. L. Dewald, T. R. Dittrich, M. J. Edwards, W. A. Farmer, J. E. Field, D. Fittinghoff, J. Frenje, J. Gaffney, M. Gatu Johnson, S. H. Glenzer, G. P. Grim, S. Haan, K. D. Hahn, G. N. Hall, B. A. Hammel, J. Harte, E. Hartouni, J. E. Heebner, V. J. Hernandez, H. Herrmann, M. C. Herrmann, D. E. Hinkel, D. D. Ho, J. P. Holder, W. W. Hsing, H. Huang, K. D. Humbird, N. Izumi, L. C. Jarrott, J. Jeet, O. Jones, G. D. Kerbel, S. M. Kerr, S. F. Khan, J. Kilkenny, Y. Kim, H. Geppert Kleinrath, V. Geppert Kleinrath, C. Kong, J. M. Koning, J. J. Kroll, M. K. G. Kruse, B. Kustowski, O. L. Landen, S. Langer, D. Larson, N. C. Lemos, J. D. Lindl, T. Ma, M. J. MacDonald, B. J. MacGowan, A. J. Mackinnon, S. A. MacLaren, A. G. MacPhee, M. M. Marinak, D. A. Mariscal, E. V. Marley, L. Masse, K. Meaney, N. B. Meezan, P. A. Michel, M. Millot, J. L. Milovich, J. D. Moody, A. S. Moore, J. W. Morton, T. Murphy, K. Newman, J.-M. G. Di Nicola, A. Nikroo, R. Nora, M. V. Patel, L. J. Pelz, J. L. Peterson, Y. Ping, B. B. Pollock, M. Ratledge, N. G. Rice, H. Rinderknecht, M. Rosen, M. S. Rubery, J. D. Salmonson, J. Sater, S. Schiaffino, D. J. Schlossberg, M. B. Schneider, C. R.

- Schroeder, H. A. Scott, S. M. Sepke, K. Sequoia, M. W. Sherlock, S. Shin, V. A. Smalyuk, B. K. Spears, P. T. Springer, M. Stadermann, S. Stoupin, D. J. Strozzi, L. J. Suter, C. A. Thomas, R. P. J. Town, E. R. Tubman, C. Trosseille, P. L. Volegov, C. R. Weber, K. Widmann, C. Wild, C. H. Wilde, B. M. Van Wonterghem, D. T. Woods, B. N. Woodworth, M. Yamaguchi, S. T. Yang, and G. B. Zimmerman, Burning plasma achieved in inertial fusion, *Nature* **601**, 542–548 (2022).
- [4] B. D. Keenan, W. T. Taitano, A. N. Simakov, L. Chacón, and B. J. Albright, Shock-driven kinetic and diffusive mix in high- z pusher icf designs, *Physics of Plasmas* **27**, 10.1063/1.5140361 (2020).
- [5] D. S. Clark, A. Allen, S. H. Baxamusa, J. Biener, M. M. Biener, T. Braun, S. Davidovits, L. Divol, W. A. Farmer, T. Fehrenbach, C. Kong, M. Millot, J. Milovich, A. Nikroo, R. C. Nora, A. E. Pak, M. S. Rubery, M. Stadermann, P. Sterne, C. R. Weber, and C. Wild, Modeling ablator defects as a source of mix in high-performance implosions at the national ignition facility, *Physics of Plasmas* **31**, 10.1063/5.0200730 (2024).
- [6] K. O. Mikaelian, Richtmyer-meshkov instabilities in stratified fluids, *Phys. Rev. A* **31**, 410 (1985).
- [7] T. Sano, K. Ishigure, and F. Cobos-Campos, Suppression of the richtmyer-meshkov instability due to a density transition layer at the interface, *Physical Review E* **102**, 10.1103/physreve.102.013203 (2020).
- [8] Y. Liang and X. Luo, Shock-induced dual-layer evolution, *Journal of Fluid Mechanics* **929**, 10.1017/jfm.2021.903 (2021).
- [9] W. J. Schill, M. R. Armstrong, J. H. Nguyen, D. M. Sterbentz, D. A. White, L. X. Benedict, R. N. Rieben, A. Hoff, H. E. Lorenzana, J. L. Belof, B. M. La Lone, and M. D. Staska, Suppression of richtmyer-meshkov instability via special pairs of shocks and phase transitions, *Phys. Rev. Lett.* **132**, 024001 (2024).
- [10] R. Samtaney, Suppression of the richtmyer–meshkov instability in the presence of a magnetic field, *Physics of Fluids* **15**, L53–L56 (2003).
- [11] T. Sano, T. Inoue, and K. Nishihara, Critical magnetic field strength for suppression of the richtmyer-meshkov instability in plasmas, *Physical Review Letters* **111**, 10.1103/physrevlett.111.205001 (2013).
- [12] C. M. Huntington, A. Shimony, M. Trantham, C. C. Kuranz, D. Shvarts, C. A. Di Stefano, F. W. Doss, R. P. Drake, K. A. Flippo, D. H. Kalantar, S. R. Klein, J. L. Kline, S. A. MacLaren, G. Malamud, A. R. Miles, S. T. Prsbrey, K. S. Raman, B. A. Remington, H. F. Robey, W. C. Wan, and H.-S. Park, Ablative stabilization of rayleigh-taylor instabilities resulting from a laser-driven radiative shock, *Physics of Plasmas* **25**, 10.1063/1.5022179 (2018).
- [13] S. W. Haan, J. D. Lindl, D. A. Callahan, D. S. Clark, J. D. Salmonson, B. A. Hammel, L. J. Atherton, R. C. Cook, M. J. Edwards, S. Glenzer, A. V. Hamza, S. P. Hatchett, M. C. Herrmann, D. E. Hinkel, D. D. Ho, H. Huang, O. S. Jones, J. Kline, G. Kyrala, O. L. Landen, B. J. MacGowan, M. M. Marinak, D. D. Meyerhofer, J. L. Milovich, K. A. Moreno, E. I. Moses, D. H. Munro, A. Nikroo, R. E. Olson, K. Peterson, S. M. Pollaine, J. E. Ralph, H. F. Robey, B. K. Spears, P. T. Springer, L. J. Suter, C. A. Thomas, R. P. Town, R. Vesey, S. V. Weber, H. L. Wilkens, and D. C. Wilson, Point design targets, specifications, and requirements for the 2010 ignition campaign on the national ignition facility, *Physics of Plasmas* **18**, 10.1063/1.3592169 (2011).
- [14] R. B. Randolph, J. A. Oertel, D. W. Schmidt, M. N. Lee, B. M. Patterson, K. C. Henderson, and C. E. Hamilton, Process development and micro-machining of marble foam-cored rexolite hemi-shell ablator capsules, *Fusion Science and Technology* **70**, 230–236 (2016).
- [15] R. E. Olson, T. J. Murphy, B. M. Haines, M. R. Douglas, B. J. Albright, M. A. Gunderson, Y. Kim, T. Cardenas, C. E. Hamilton, and R. B. Randolph, Development of the marble experimental platform at the national ignition facility, *Physics of Plasmas* **27**, 10.1063/5.0018819 (2020).
- [16] N. N. Vazirani, R. Sacks, B. M. Haines, M. J. Grosskopf, D. J. Stark, and P. A. Bradley, Bayesian batch optimization for molybdenum versus tungsten inertial confinement fusion double shell target design, *Statistical Analysis and Data Mining: The ASA Data Science Journal* **17**, 10.1002/sam.11698 (2024).
- [17] J. J. Kuczek and B. M. Haines, Simulated impact of fill tube geometry on recent high-yield implosions at the national ignition facility, *Physics of Plasmas* **30**, 10.1063/5.0156346 (2023).
- [18] B. M. Haines, W. S. Daughton, E. N. Loomis, E. C. Merritt, D. S. Montgomery, J. P. Sauppe, and J. L. Kline, Computational study of instability and fill tube mitigation strategies for double shell implosions, *Physics of Plasmas* **26**, 10.1063/1.5115031 (2019).
- [19] K. L. Baker, C. A. Thomas, T. R. Dittrich, O. Landen, G. Kyrala, D. T. Casey, C. R. Weber, J. Milovich, D. T. Woods, M. Schneider, S. F. Khan, B. K. Spears, A. Zylstra, C. Kong, J. Crippen, N. Alfonso, C. B. Yeaman, J. D. Moody, A. S. Moore, N. B. Meezan, A. Pak, D. N. Fittinghoff, P. L. Volegov, O. Hurricane, D. Callahan, P. Patel, and P. Amendt, Fill tube dynamics in inertial confinement fusion implosions with high density carbon ablators, *Physics of Plasmas* **27**, 10.1063/5.0011385 (2020).
- [20] C. R. Weber, D. S. Clark, A. Pak, N. Alfonso, B. Bachmann, L. F. Berzak Hopkins, T. Bunn, J. Crippen, L. Divol, T. Dittrich, A. L. Kritcher, O. L. Landen, S. Le Pape, A. G. MacPhee, E. Marley, L. P. Masse, J. L. Milovich, A. Nikroo, P. K. Patel, L. A. Pickworth, N. Rice, V. A. Smalyuk, and M. Stadermann, Mixing in icf implosions on the national ignition facility caused by the fill-tube, *Physics of Plasmas* **27**, 10.1063/1.5125599 (2020).
- [21] C. Zulick, Y. Aglitskiy, M. Karasik, A. J. Schmitt, A. L. Velikovich, and S. P. Obenschain, Multimode hydrodynamic instability growth of preimposed isolated defects in ablatively driven foils, *Phys. Rev. Lett.* **125**, 055001 (2020).
- [22] I. V. Igumenshchev, V. N. Goncharov, W. T. Shmayda, D. R. Harding, T. C. Sangster, and D. D. Meyerhofer, Effects of local defect growth in direct-drive cryogenic implosions on omega, *Physics of Plasmas* **20**, 082703 (2013).
- [23] D. Eriksson, M. Pearce, J. R. Gardner, R. D. Turner, and M. Poloczek, Scalable global optimization via local bayesian optimization, *arXiv e-prints* 10.48550/arXiv.1910.01739 (2019), arXiv:1910.01739 [cs.LG].
- [24] D. M. Sterbentz, C. F. Jekel, D. A. White, S. Aubry, H. E. Lorenzana, and J. L. Belof, Design optimization for richtmyer–meshkov instability suppression at shock-compressed material interfaces, *Physics of Fluids* **34**,

- 10.1063/5.0100100 (2022).
- [25] Y. Aglitskiy, M. Karasik, A. L. Velikovich, V. Serlin, J. L. Weaver, T. J. Kessler, S. P. Nikitin, A. J. Schmitt, S. P. Obenschain, N. Metzler, and J. Oh, Observed transition from richtmyer-meshkov jet formation through feedout oscillations to rayleigh-taylor instability in a laser target, *Physics of Plasmas* **19**, 102707 (2012).
- [26] Y. Aglitskiy, A. L. Velikovich, M. Karasik, V. Serlin, C. J. Pawley, A. J. Schmitt, S. P. Obenschain, A. N. Mostovych, J. H. Gardner, and N. Metzler, Direct observation of mass oscillations due to ablative richtmyer-meshkov instability in plastic targets, *Phys. Rev. Lett.* **87**, 265001 (2001).
- [27] Y. Aglitskiy, A. L. Velikovich, M. Karasik, V. Serlin, C. J. Pawley, A. J. Schmitt, S. P. Obenschain, A. N. Mostovych, J. H. Gardner, and N. Metzler, Direct observation of mass oscillations due to ablative richtmyer-meshkov instability and feedout in planar plastic targets, *Physics of Plasmas* **9**, 2264 (2002).
- [28] F. Christ, G. Schaumann, N. Schott, J. Vetter, A. Blaeser, and M. Roth, Two-photon polymerization for inertial fusion energy target fabrication, *Applied Physics A* **131**, 10.1007/s00339-025-08657-x (2025).
- [29] S. Pandolfi, T. Carver, D. Hodge, A. F. T. Leong, K. Kurzer-Ogul, P. Hart, E. Galtier, D. Khaghani, E. Cunningham, B. Nagler, H. J. Lee, C. Bolme, K. Ramos, K. Li, Y. Liu, A. Sakdinawat, S. Marchesini, P. M. Kozlowski, C. B. Curry, F.-J. Decker, S. Vetter, J. Shang, H. Aluie, M. Dayton, D. S. Montgomery, R. L. Sandberg, and A. E. Gleason, Novel fabrication tools for dynamic compression targets with engineered voids using photolithography methods, *Review of Scientific Instruments* **93**, 103502 (2022).
- [30] C. Parisuaña, M. P. Valdivia, V. Bouffetier, K. Kurzer-Ogul, G. Pérez-Callejo, S. Bott-Suzuki, A. Casner, N. S. Christiansen, N. Czaplá, D. Eder, E. Galtier, S. H. Glenzer, T. Goudal, B. M. Haines, D. Hodge, M. Ikeya, L. Izquierdo, D. Khaghani, Y. Kim, S. Klein, A. Koniges, H. J. Lee, M. Leininger, A. F. T. Leong, R. S. Lester, M. Makita, D. Mancelli, W. M. Martin, B. Nagler, R. L. Sandberg, A. Truong, M. Vescovi, A. E. Gleason, and P. M. Kozlowski, Shock propagation in aerogel and tpp foams for inertial fusion energy target design, *Physics of Plasmas* **32**, 082707 (2025).
- [31] D. S. Hodge, A. F. T. Leong, K. Kurzer-Ogul, S. Pandolfi, D. S. Montgomery, J. Shang, H. Aluie, S. Marchesini, Y. Liu, K. Li, A. Sakdinawat, E. C. Galtier, B. Nagler, H. J. Lee, E. F. Cunningham, T. E. Carver, C. A. Bolme, K. J. Ramos, D. Khaghani, P. M. Kozlowski, A. E. Gleason, and R. L. Sandberg, Single-shot in-line x-ray phase-contrast imaging of void-shockwave interactions in fusion energy materials, *Physics of Plasmas* **32**, 083903 (2025).
- [32] E. M. Escauriza, J. P. Duarte, D. J. Chapman, M. E. Rutherford, L. Farbaniec, J. C. Jonsson, L. C. Smith, M. P. Olbinado, J. Skidmore, P. Foster, T. Ringrose, A. Rack, and D. E. Eakins, Collapse dynamics of spherical cavities in a solid under shock loading, *Scientific Reports* **10**, 10.1038/s41598-020-64669-y (2020).
- [33] D. Ranjan, J. Oakley, and R. Bonazza, Shock-bubble interactions, *Annual Review of Fluid Mechanics* **43**, 117–140 (2011).
- [34] D. Maler, O. Belozerov, A. Godinger, S. Efimov, J. Strucka, Y. Yao, K. Mughal, B. Lukic, A. Rack, S. N. Bland, and Y. E. Krasik, Multi frame radiography of supersonic water jets interacting with a foil target, *Journal of Applied Physics* **135**, 10.1063/5.0186659 (2024).
- [35] V. I. Oreshkin and R. B. Baksht, Wire explosion in vacuum, *IEEE Transactions on Plasma Science* **48**, 1214–1248 (2020).
- [36] G. T. Bokman, S. Fiorini, J. Strucka, B. Lukić, S. N. Bland, K. Mughal, S. Liu, A. Rack, and O. Supponen, Planar shock-induced bubble collapse and jetting in water captured via x-ray phase contrast imaging, *Applied Physics Letters* **127**, 014102 (2025).
- [37] J. Strucka, B. Lukic, M. Koerner, J. W. D. Halliday, Y. Yao, K. Mughal, D. Maler, S. Efimov, J. Skidmore, A. Rack, Y. Krasik, J. Chittenden, and S. N. Bland, Synchrotron radiography of richtmyer–meshkov instability driven by exploding wire arrays, *Physics of Fluids* **35**, 10.1063/5.0144839 (2023).
- [38] M. P. Olbinado, X. Just, J.-L. Gelet, P. Lhuissier, M. Scheel, P. Vagovic, T. Sato, R. Graceffa, J. Schulz, A. Mancuso, J. Morse, and A. Rack, MHz frame rate hard x-ray phase-contrast imaging using synchrotron radiation, *Optics Express* **25**, 13857 (2017).
- [39] M. P. Olbinado, V. Cantelli, O. Mathon, S. Pascarelli, J. Grenzer, A. Pelka, M. Roedel, I. Prencipe, A. L. Garcia, U. Helbig, D. Kraus, U. Schramm, T. Cowan, M. Scheel, P. Pradel, T. D. Resseguier, and A. Rack, Ultra high-speed x-ray imaging of laser-driven shock compression using synchrotron light, *Journal of Physics D: Applied Physics* **51**, 055601 (2018).
- [40] S. Bakhrakh, O. Drennov, and N. Kovalev, *Hydrodynamic instability in strong media* (1997).
- [41] R. Anderson, A. Black, B. Blakeley, R. Bleile, J.-S. Camier, J. Ciurej, A. Cook, V. Dobrev, N. Elliott, J. Grondalski, C. Harrison, R. Hornung, T. Kolev, M. Legendre, W. Liu, W. Nissen, B. Olson, M. Osawe, G. Papadimitriou, O. Pearce, R. Pember, A. Skinner, D. Stevens, T. Stitt, L. Taylor, V. Tomov, R. Rieben, A. Vargas, K. Weiss, D. White, and L. Busby, *The Multi-physics on Advanced Platforms Project*, Tech. Rep. Tech. rep., LLNL-TR-815869 (Lawrence Livermore National Laboratory, Livermore, CA (United States), 2020).
- [42] R. Rieben, Poster: The MARBL multi-physics code, in *Exascale Computing Project Annual Meeting* (2020).
- [43] R. W. Anderson, V. A. Dobrev, T. V. Kolev, R. N. Rieben, and V. Z. Tomov, High-order multi-material ALE hydrodynamics, *SIAM J. Sci. Comput.* **40**, B32 (2018).
- [44] G. Dimonte, G. Terrones, F. J. Cherne, T. C. Germann, V. Dupont, K. Kadau, W. T. Buttler, D. M. Oro, C. Morris, and D. L. Preston, Use of the Richtmyer–Meshkov instability to infer yield stress at high-energy densities, *Phys. Rev. Lett.* **107**, 264502 (2011).
- [45] D. M. Sterbentz, C. F. Jekel, D. A. White, R. N. Rieben, and J. L. Belof, Linear shaped-charge jet optimization using machine learning methods, *Journal of Applied Physics* **134**, 10.1063/5.0156373 (2023).
- [46] M. B. Prime, S. J. Fensin, D. R. Jones, J. W. Dyer, and D. T. Martinez, Multiscale richtmyer-meshkov instability experiments to isolate the strain rate dependence of strength, *Physical Review E* **109**, 10.1103/physreve.109.015002 (2024).